El Niño-related stratification anomalies over the continental slope off Oregon in summer 2014 and 2015

Alexander L. Kurapov[1]

[1]National Oceanic and Atmospheric Administration/National Ocean Service/Office of Coast Survey/Coast Survey Development Laboratory/Coastal Marine Modeling Branch, Silver Spring, Maryland, USA, 20910

Key Points:

- In summer 2014 and 2015, the ocean circulation model and data reveal episodes of anomalously weak stratification over the continental slope off Oregon
- Advection of the seasonal potential vorticity gradient by the anomalously strong slope current drives the weaker stratification anomaly
- The poleward along-slope current anomaly is part of the El Niño oceanic response propagated with coastally trapped waves

Corresponding author: Alexander L. Kurapov, `Alexander.Kurapov@noaa.gov`

Abstract

Over the continental slope off Oregon at the US West Coast, at 44.6N, vertical stratification is found to be anomalously weak in July-August of 2014 and 2015 both in a regional ocean circulation model and Conductivity-Temperature-Depth (CTD) profile observations. To understand the responsible mechanism, we focus on the layer between the isopycnal surfaces $\sigma_\theta = 26.5$ and 26.25 kg m^{-3} that is found between depths 100-300 m and represents material properties characteristic of the slope poleward undercurrent and shelf-slope exchange. This layer thickness, about 50 m on average, can be twice as large during the above-mentioned periods. In the 2009-2018 model analysis, this anomaly is revealed over the continental slope only in summers 2014 and 2015 and only off the Oregon and Washington coasts (40-47N). The stratification anomaly is explained as the effect of advection of the seasonal alongslope potential vorticity (PV) gradient by an anomalously strong poleward slope current. In the annual cycle, the zone of strong alongslope PV gradient is found between 40-47N, supported by the local upwelling that results in the injection of the large PV in the bottom boundary layer over the shelf followed by its offshore transport in the slope region. The positive alongslope current anomaly propagates to Oregon with coastally trapped waves as part of the El Niño oceanic response and can be up to 0.1 m s^{-1}. Advection by this anomalous poleward current results in transporting the seasonal PV gradient earlier in the season than on average.

Plain Language Summary

Understanding the oceanic dynamics along the continental slopes is important for understanding material exchanges between the coastal and interior ocean and biological diversity. Analysis of a high-resolution, three-dimensional ocean circulation model helps explain observed variability over the slope. Associated with the global anomaly pattern called El Niño, the along-slope poleward current off Oregon was anomalously strong in summers 2014 and 2015. This anomalous transport caused alongshore displacement of the water masses from the south resulting in the vertical spreading of the subsurface oceanic layers.

1 Introduction

Seasonal ocean variability along the large part of the US West Coast, between Point Conception and Juan de Fuca Strait (Figure 1), is dominated by strong wind-driven up-

welling in summer and downwelling in winter (Huyer, 1983; Hickey, 1998; Austin & Barth, 2002; Durski et al., 2015). Upwelling supports an energetic surface intensified southward coastal current, frontal instabilities, eddy generation, and jet separation that contribute to the shelf-interior ocean momentum, heat and material exchange (Kosro et al., 1991; Barth & Smith, 1998; Durski & Allen, 2005; Koch et al., 2010). In June-July each year, a poleward undercurrent develops along the continental slope (Pierce et al., 2000; Collins et al., 2013; Connolly et al., 2014; Molemaker et al., 2015). It is about 25-50 km wide and its core is found between 100-300 m depths. Samelson (2017) explains the undercurrent as part of the offshore-propagating planetary wave response following the upwelling conditions setup at the coast.

Coastal ocean variability in this region is influenced by basin scale oceanic and atmospheric anomalies. As a recent example, one of the strongest heat waves on the record hit the North-Eastern Pacific (NEP) region in 2014-2016. It was influenced by the emergence of the "warm blob" pattern in the Gulf of Alaska early in 2014 followed by a major El Niño that tried to break through early in 2014, then "fizzled" and reemerged as a major event in 2015 (Bond et al., 2015; McPhaden, 2015; Rudnick et al., 2021; Amaya et al., 2016; Di Lorenzo & Mantua, 2016; Jacox et al., 2016; Peterson et al., 2017; Jacox et al., 2019). Kurapov et al. (2022) studied impacts of this El Niño on the coastal ocean dynamics along the US West Coast using a ten-year, 2009-2018, regional ocean model simulation in the domain shown in Fig. 1a. Additional analyses using this model are presented in this paper. The model horizontal resolution is 2 km, which allows it to represent the dynamics driving shelf, slope and interior flows. The model-data comparisons demonstrate that the model reproduces correctly variability on time scales from several days to seasonal and interannual. In particular, the model reproduces the El Niño major features including the wide-spread warming of the surface layer, coastal sea level rising, and anomalous deepening of the isopycnal surfaces over the slope (Zaba & Rudnick, 2016; Zaba et al., 2020). In summer 2014 and 2015, the flow over the shelf and slope off Oregon (40-46N) can be explained as a superposition of the seasonal wind-driven upwelling and the El Niño-related downwelling motion that propagates from the southern boundary of the model domain as coastally trapped waves, CTW (Brink, 1991). The upwelling-favorable southward winds in summers 2014 and 2015 are close to average and hence the offshore near-surface transport is close to average. At the same time, the near-bottom cross-shelf current exhibits an offshore anomaly (i.e., the onshore transport is weakened

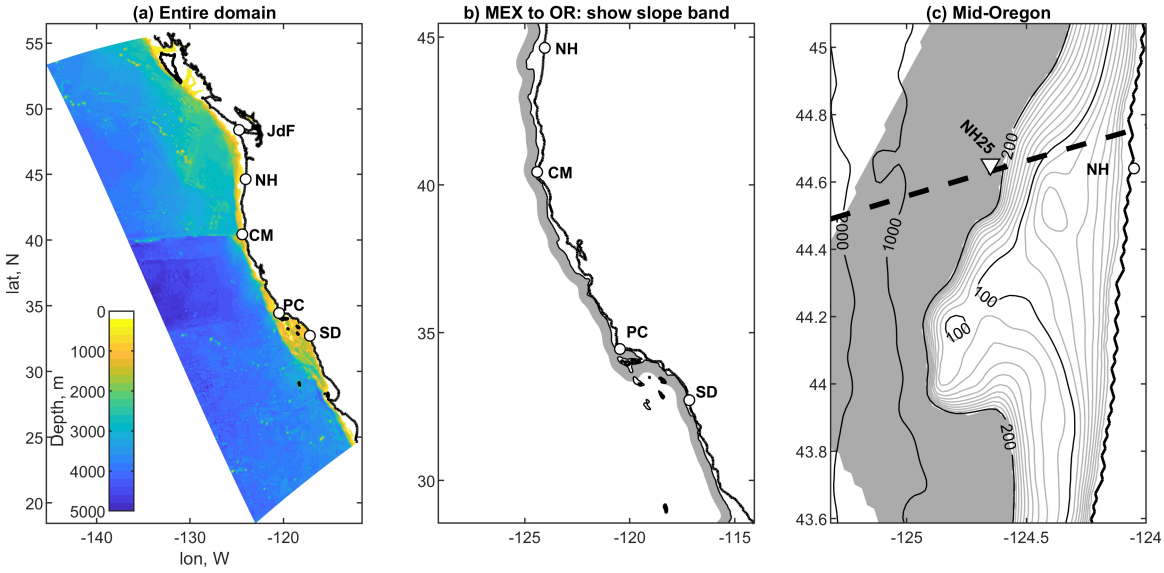

Figure 1. Maps: (a) The entire model domain, color: bathymetry; (b) a close-up on the slope area from Mexico to Oregon, to show the slope band (half-tone), defined as an area 0-40 km offshore of the 200-m isobath (black); (c) a close-up on the mid-Oregon shelf, bathymetric contours are (black) 100, 200, 1000 and 2000 m and (half-tone) from 10 to 190 m every 10 m; NH25 is the location of the ship CTD station and the dashed line is the model section (see Fig. 3 and 6); gray: the slope band. In (a)-(c), circles show geographic reference points: San Diego (SD, 32.7N), Point Conception (PC, 34.4N), Cape Mendocino (CM, 40.4N), Newport, OR (NH, 44.6N), and Juan de Fuca Strait (JdF, 48.4N).

or reversed toward offshore). The alongshore current component over the shelf, usually southward in Oregon, is anomalously weak. Over the slope, the poleward velocity anomaly adds to the undercurrent. This anomaly is connected to the anomalies near the southern boundary at 24N that propagate all along the slope with the speed of approximately 2.5 m s^{-1} characteristic of CTW.

The 10-year model simulation at the 2-km resolution shows very rich behavior over a wide spectrum of temporal and spatial scales and provides a tool to reveal new anomalies and dynamical effects. In the present study, we utilize the same model solution to explain episodes of weaker stratification detected over the continental slope off Oregon in summer 2014 and 2015, both in the model and available observations. This stratification anomaly will be explained as the effect of anomalous poleward advection of the

seasonal alongslope gradient of the potential vorticity (PV). This will be an example where a local anomaly is forced by a combination of a remote forcing (as the poleward slope current anomaly propagates to the study area with CTW) and a more local, advective mechanism. Explaining this effect will improve our understanding of how the shelf and slope interact.

2 The model and methods

All the model implementation details can be found in (Kurapov et al., 2022) and only a short summary is provided here. The model is based on the Regional Ocean Modeling System, ROMS (www.myroms.org), a three-dimensional model describing the nonlinear evolution of the stratified ocean. The model domain (Figure 1a) extends along the coast from 24N to 54N, including part of the Mexican coast, all of the US and most of the British Columbia, Canada coasts. The resolution is 2 km in the horizontal and 40 terrain-following levels in the vertical direction. The vertical dicretization is relatively better near the surface and bottom such that, e.g., the top 50 m are resolved by nine or more layers everywhere; over the shelf, inshore of the 200 m isobath, the bottom 20 m are represented by four or more levels. The vertical coordinate z is directed upward and the mean free surface is near 0; accordingly, the depths of isopycnal surfaces will be reported below as $z_\sigma < 0$. Model atmospheric fluxes are computed using ECMWF ERA5 fields (ECMWF: European Center for Medium-Range Weather Forecasts, ERA: ECMWF Reanalysis). Non-tidal oceanic boundary conditions are obtained from the HYCOM global US Navy nowcasts (www.hycom.org). The barotropic tidal boundary conditions are added using dominant harmonic constituents from the Pacific regional TPXO estimate (https://www.tpxo.net/regional, (Egbert & Erofeeva, 2002)). The model simulation period is 1 October, 2008 – 25 October, 2018. Analyses presented below use daily averaged outputs.

The model does not assimilate any data inside the domain and provides a continuous, dynamically and thermodynamically balanced solution driven only by the atmospheric and oceanic boundary fluxes, which is most suitable for process studies.

Some of the analyses below are provided for the across-slope-averaged variables. The approximately 40-km wide slope band is defined just offshore of the 200-m isobath (shaded areas in Fig. 1b and c). This band width is chosen to be close to the width of the poleward undercurrent (Pierce et al., 2000). The subsurface alongslope velocity v_s

is defined as in (Kurapov et al., 2022) by projecting the horizontal velocity vectors in cross-slope sections onto the alongslope direction and averaging in the horizontal across the band and in the vertical between depths of $z = -300$ and -125 m, where the core of the undercurrent is expected to be found. $v_s(y,t)$ is positive toward the north and is a function of the alongslope coordinate (precisely, the alongslope distance from the southern boundary) y and time t.

The PV is introduced in geophysical fluid dynamics as a dynamical tracer related to vorticity that is conserved following a fluid element under conditions having no dissipation, mixing or external boundary fluxes. In the most general form (Pedlosky, 1987):

$$PV = \boldsymbol{\omega}_a \cdot \frac{\nabla \lambda}{\rho}, \tag{1}$$

where $\boldsymbol{\omega}_a$ is the absolute vorticity vector and $\lambda = \lambda(p, \rho)$, a function of pressure p and density ρ, is conserved for a fluid element. If $\lambda = \sigma_\theta$ (the potential density), then the PV flux across the isopycnal surfaces is 0 even in presence of momentum dissipation and mixing in the ocean interior (Haynes & McIntyre, 1987, 1990). The PV can be injected in the layer between two isopycnal surfaces only at the atmosphere-ocean interface if the layer is outcropped (Marshall & Nurser, 1992; Thomas, 2005) or at the sloping ocean bottom (Hallberg & Rhines, 2000; Williams & Roussenov, 2003; Bethuysen & Thomas, 2012; Pringle, 2022).

An approximation to PV adopted in this study will use only the local vertical component of the absolute vorticity (Bethuysen & Thomas, 2012):

$$q = (f + \omega)N^2 = (f + \omega)\left(-\frac{g}{\rho_0}\frac{\partial \sigma_\theta}{\partial z}\right), \tag{2}$$

where $\omega = \hat{z} \cdot (\nabla \times \boldsymbol{u})$ is the vertical component of the relative vorticity, $\hat{z}$ the vertical unit vector, $\boldsymbol{u}$ the current vector, N the buoyancy frequency, g gravity, and ρ_0 reference density. In our analyses we will present q (2) on isopycnal surfaces and in the vertical sections. While the relative vorticity is an important contributor to the PV in the vicinity of the slope boundary (Molemaker et al., 2015), subsurface flows away from the boundary are in nearly geostrophic balance, $\omega/f \ll 1$, at least on the horizontal scales resolved by our model. To estimate the cross-slope-band averaged, vertically averaged PV between two selected isopycnal surfaces, specifically $\sigma_\theta = 26.5$ and 26.25 kg m^{-3}, the background

147 PV is used that neglects ω (McDowell et al., 1982; O'Dwyer & Williams, 1997; Kurapov
148 et al., 2017b):

$$q_B = f\frac{g}{\rho_0}\frac{\Delta\sigma_\theta}{\Delta z}, \tag{3}$$

149 where $\Delta\sigma_\theta = 0.25$ kg m^{-3} and $\Delta z = z_{26.25} - z_{26.5}$ is the vertical distance between
150 the selected surfaces. Generally over the slope, $-300 < z_{26.5} < -175$ m and $z_{26.25}$ is
151 found about 50 m above $z_{26.5}$ (Kurapov et al., 2017b). So, over the slope region, the range
152 of depths between $z_{26.5}$ and $z_{26.25}$ is within the limits of -300 and -125 m used in the
153 definition of the alongslope current $v_s(y,t)$.

154 In this paper we will discuss cross-band-slope averaged variables $z_{26.5}(y,t)$, $z_{26.25}(y,t)$,
155 $q_B(y,t)$, and $v_s(y,t)$. To reduce the "noise" due to the slope eddies, a Gaussian filter with
156 the 100-km correlation length scale is applied to these functions in the y direction.

157 Time series analyses involve computation of the annual cycle and anomalies. The
158 annual cycle is defined by fitting the linear combination of the mean and three harmon-
159 ics with the periods of 1, 1/2, and 1/3 year to the time series using the pre-heat-wave
160 years 2009-2013. Kurapov et al. (2022) show that the poleward undercurrent is the salient
161 feature of the $v_s(y,t)$ annual cycle, peaking in Oregon at the end of July with the speed
162 of 0.07 m s^{-1}.

163 To provide observational evidence of episodes of the reduced stratification over the
164 slope off Oregon in the El Niño years, repeated ship CTD profile data are utilized at sta-
165 tion NH25 along the Newport Hydrographic (NH) Line (44.65N) located 25 nautical miles
166 offshore, where the total water depth is $h = 275$ m (Fisher et al., 2015; Peterson et al.,
167 2017; Risien et al., 2022) (Figure 1c). This unique time series, 1999 through present, is
168 a result of the multiyear effort led by W. Peterson, J. Fisher et al. attempting to main-
169 tain the two-week frequency of hydrographic and biogeochemical profile observations at
170 several stations at the NH line, although stations offshore of $h = 200$ m were visited
171 less often.

172 3 The stratification anomaly over the slope

173 We have already shown that $z_{26.5}$ over the slope off Oregon is anomalously deep
174 in 2014-2015 (Kurapov et al., 2022). New analyses focus on the anomalies in both $z_{26.5}$

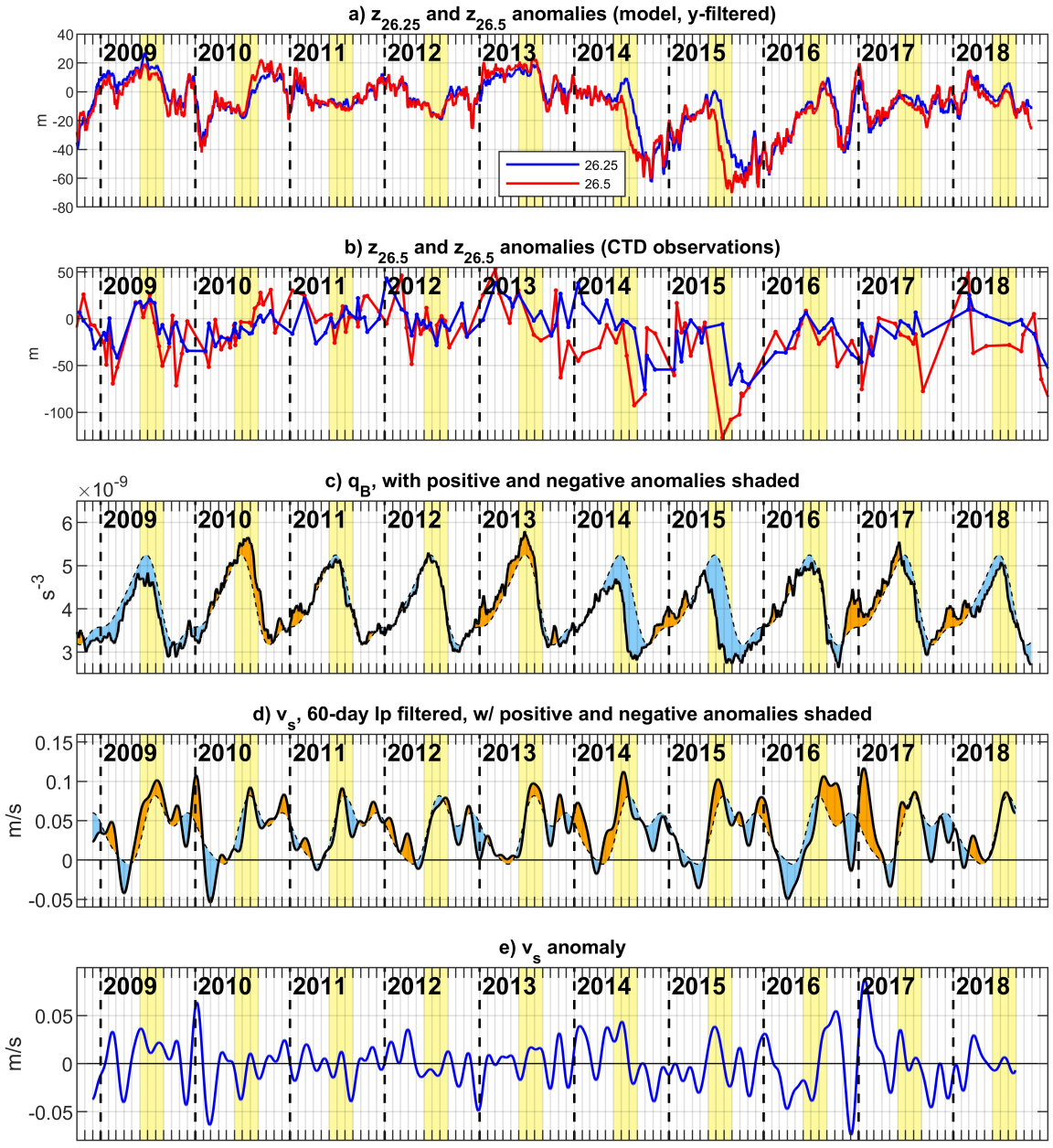

Figure 2. Time series at 44.6N: (a) model $z_{26.5}$ and $z_{26.25}$ anomalies averaged across the slope band (i.e., 0-40 km offshore of the 200-m isobath); (b) observed $z_{26.5}$ and $z_{26.25}$ anomalies, ship CTD at the NH25 station (h = 275 m), (c) solid line: model q_B averaged across the slope band, dashed line: annual cycle in q_B; (d) solid line: v_s, dashed line: annual cycle in v_s; (e) v_s anomaly. The anomalies are with respect to the annual cycle, based on 2009-2013. In (c) and (d), the orange and blue shades show positive and negative anomalies from the annual cycle. Vertical dashed lines: 1 January of each year. Yellow shades: summer months (JJA). Tick marks on the time axis are on the 1st of each month.

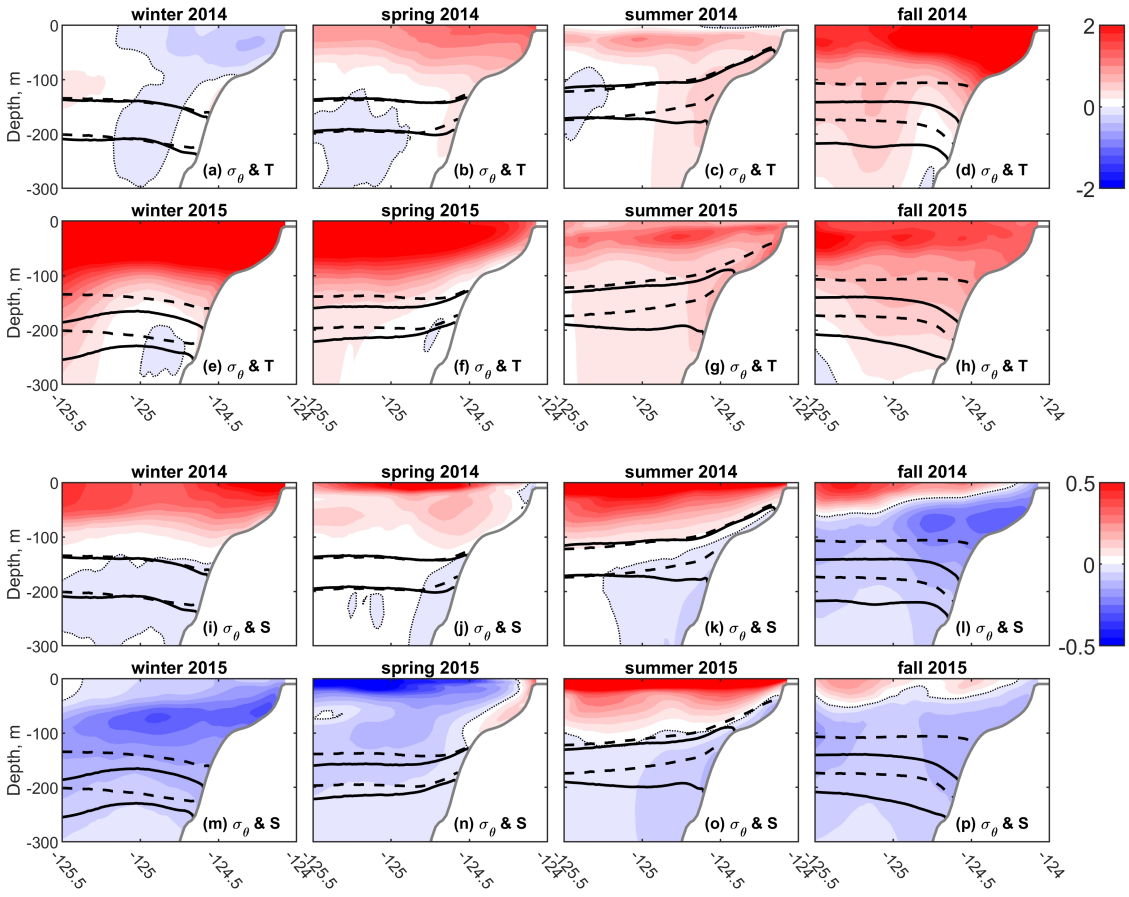

Figure 3. Black thick contours: the seasonally averaged σ_θ = 26.5 and 26.25 kg m^{-3} in 2014-2015 in the model cross-shore section near the NH line, 44.6N (see Fig. 1c for the section location): (solid) 3-month averages in 2014 and 2015, (dashed) 2009-2013 average for each season. Background color: seasonal anomalies in (rows 1-2) T (°C), (rows 3-4) S. Winter, spring, summer and fall are defined as DJF, MAM, JJA, and SON, correspondingly. The thin dotted contour shows T or S zero anomaly.

and $z_{26.25}$, averaged across the slope band (Figure 2a). These vary in unison (*i.e.*, Δz anomaly is near 0) for most of the 10-year study period. The notable exceptions are two periods, July-August of each 2014 and 2015, when not only the depth anomaly of each surface is the deepest, but also Δz is increased by about 50 m. In the NH25 CTD profile data (Fig. 2b), the separation between these layers is also anomalously large during the same time periods. In 2015, the observed local Δz anomaly is in excess of 100 m.

Over the slope off Oregon, q_B averaged between $z_{26.5}$ and $z_{26.25}$ shows a strong upwelling/downwelling annual cycle (Fig. 2c). The strongest negative anomalies are presented in summer of each 2014 and 2015, consistent with the strong Δz anomalies during the same period. Figure 3 presents this anomaly in a model cross-shore vertical section near the NH line (the section location is shown in Fig. 1c). In these section plots, the thick black contours show 3-month averaged σ_θ in 2014 and 2015 (solid lines) and seasonal climatological σ_θ (dashed lines). The background color is the seasonal T (rows 1,2) or S anomalies (rows 3,4). Both isopycnal surfaces, 26.25 and 26.5 kg m^{-3}, are near their climatological levels in winter and spring 2014 (Figure 3a,b,i,j). In summer 2014 (c,k), $z_{26.25}$ is near the climatological level supported by the upwelling favorable winds. At the same time, $z_{26.5}$ is depressed resulting in the weaker stratification anomaly over the slope. In fall 2014 (d,l), both isopycnal surfaces are about 50 m below their climatological levels, but the relative distance Δz is again close to the climatology. In winter 2015 (e,m), the isopycnal surfaces are still depressed relative to climatology. By spring 2015 (f,n), these are moved up over the slope by upwelling reaching the climatological levels over the shelf. Summer 2015 (g,o) is similar to summer 2014 showing the anomalously large spreading between the layers over the slope, mainly due to $z_{26.5}$ anomalous deepening.

In a series of plots in Figure 3a-h, it may be noticed that the $z_{26.5}$ anomaly near the slope leads the anomaly at the offshore extent of the cross-section shown. This effect can be associated with the offshore planetary wave propagation (Kurapov et al., 2022).

The near-bottom T anomaly over the shelf and slope in summers 2014 and 2015 (Fig. 3c,g) is accompanied by the fresher S anomaly (k,o) and is a signature of the El Niño-related downwelling. The extreme T anomaly, in excess of 2°C, shows in the top 100 m in fall 2014 (Fig. 3d) after the warm blob waters reach the shelf (Barth et al., 2018). The strong S anomaly extending over the shelf and slope is evident starting fall 2014. This and other details of the T and S anomalies are intriguing but require more detailed analyses and are left as a topic of future studies.

To see where along the slope the q_B anomalies reveal themselves and how they may compare to v_s, the anomalies in $v_s(y,t)$ and $q_B(y,t)$ are shown as Hovmöller diagrams. Anomalies in v_s (Figure 4a) exhibit fast propagating CTW patterns as discussed in (Kurapov et al., 2022). In spring-summer 2014 and summer 2015 episodes of sustained positive anoma-

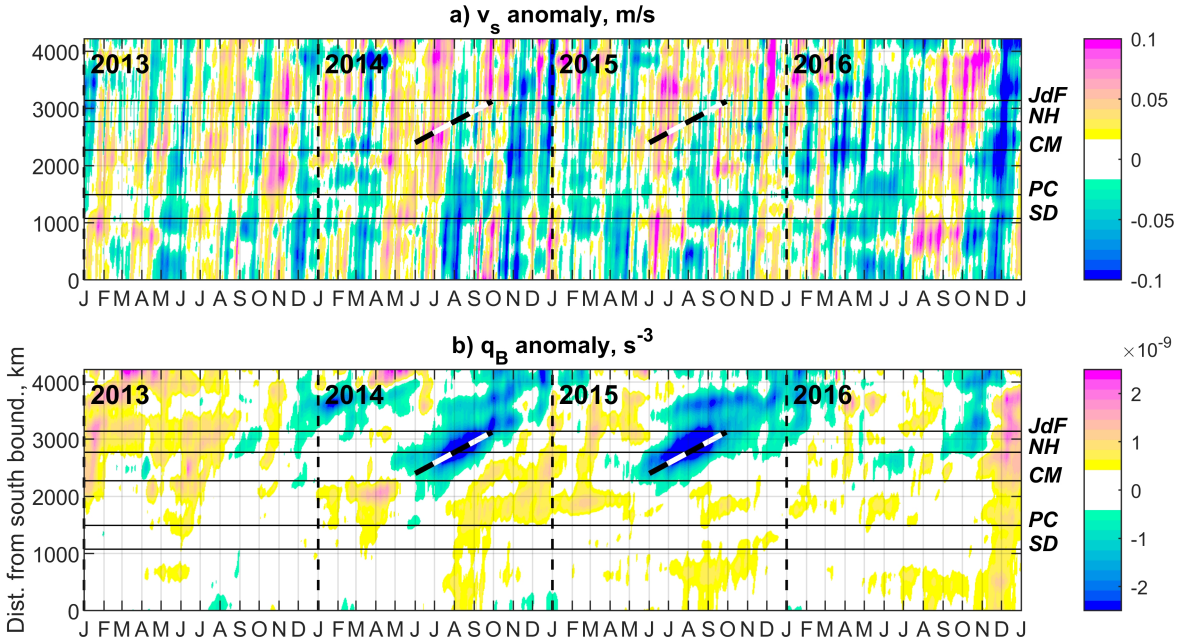

Figure 4. Time vs. alongslope distance plots of anomalies in the slope-band averaged properties, 2013-2016: (a) v_s, (b) q_B. The dashed guidelines correspond to the characteristic advective speed of 0.07 m s^{-1}. Vertical dashed lines show 1 January of each year. Horizontal lines show reference coastal points (see Fig. 1): San Diego (SD, 32.7N), Point Conception (PC, 34.4N), Cape Mendocino (CM, 40.4N), Newport, OR (NH, 44.6N), and Juan de Fuca Strait (JdF, 48.4N).

lies reaching 0.1 m s^{-1} are evident, connected to the model southern boundary. In contrast, the q_B diagram (Figure 4b) does not show the strong CTW signal. The negative anomalies of 2014 and 2015 are found only north of Cape Mendocino (CM, 40.4N) in Northern California and are the largest between CM and Juan de Fuca Strait (JdF, 48.4N), i.e. along the coasts of Oregon and Washington. In each summer, the anomalies emerge just north of CM coinciding with the time of the large positive v_s anomaly. Then the negative disturbance is transported northward with the speed of 0.07 m s^{-1} characteristic of the poleward undercurrent.

Our hypothesis is that the advection of the alongslope gradient of q by the anomalously strong v_s drives the summer 2014 and 2015 q_B anomalies. In the symbolic form, the dominant balance is as follows:

$$\frac{\partial q_B}{\partial t} \approx -v_s \frac{\partial q_B}{\partial y}. \tag{4}$$

This balance will be tested below (section 5). We already noted in the introduction that v_s was anomalously strong during those periods. The time series of the total v_s, its annual cycle, and the anomaly at the NH latitude (Figure 2d,e) show that although the anomalies are not standing out as uniquely large in summer 2014 and 2015, they turn out to be the largest among all the summers. It is possible that not only the anomaly magnitude is important but also its longevity and timing relative to the peak of v_s in the annual cycle. Given the relatively modest speeds at the level of the undercurrent, to make the alongslope advection in the isopycnal layer a significant contributor to the tendency in q_B (4), the anomaly in v_s must be accompanied by the strong enough $\partial q_B/\partial y$.

4 The seasonal alongslope PV gradient

The annual cycle in $q_B(y,t)$ (Figure 5) does indeed show a zone of strong $\partial q_B/\partial y$ that undulates between CM in summer and an area north of JdF in winter. q_B increases sharply and almost simultaneously in the area between CM-JdF in April, coinciding with the beginning of the upwelling season. With the onset of the undercurrent in June-July, the zone of the large gradient starts drifting from CM to JdF with the speed of a few cm s^{-1}. Notably, the large seasonal gradient $\partial q_B/\partial y$ is found in the same area where q_B anomalies are detected in 2014 and 2015.

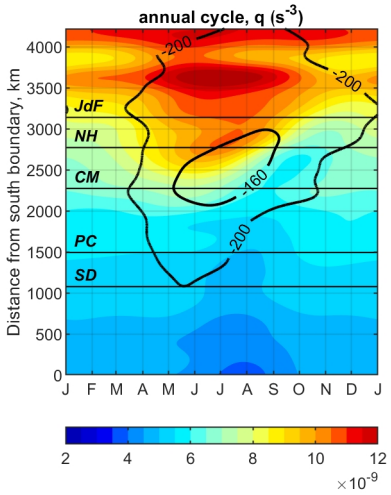

Figure 5. The annual cycle in $q_B(y)$. Black contours: annual cycle in $z_{26.5} = -200, -160$ m. Horizontal lines show reference coastal points (see Fig. 1): San Diego (SD, 32.7N), Point Conception (PC, 34.4N), Cape Mendocino (CM, 40.4N), Newport, OR (NH, 44.6N), and Juan de Fuca Strait (JdF, 48.4N).

The reason for the sharply higher q_B in the area of strong upwelling in summers is found to be due to the PV injection in the bottom boundary layer (BBL) over the sloping shelf bottom (Bethuysen & Thomas, 2012) followed by the PV anomaly entrainment from the shelf BBL to the interior layer over the slope. Physically, the PV injection across the sloping bottom during upwelling can be explained first as the geometric effect of the increase in N the near bottom. Second, the strong tendency toward BBL arrest takes place (MacCready & Rhines, 1991, 1993; Garrett et al., 1993). As part of this process the horizontal density gradient established in the BBL due to upwelling is balanced by the vertical shear in the alongshore velocity component such that the alongshore current is reduced near the bottom. As a result, the cross-shore horizontal velocity gradient is established between points in the BBL and points above the BBL farther offshore such that $\omega > 0$ near the bottom. So, both N and ω contribute to the increase in q (2) in the BBL over the sloping bottom.

To illustrate that our model represents this process, q is shown together with the the daily averaged alongslope velocity in the NH cross-shore section (Figure 6). For example, on March 31, 2011 (Fig. 6a,c), before the onset of the first upwelling event of the

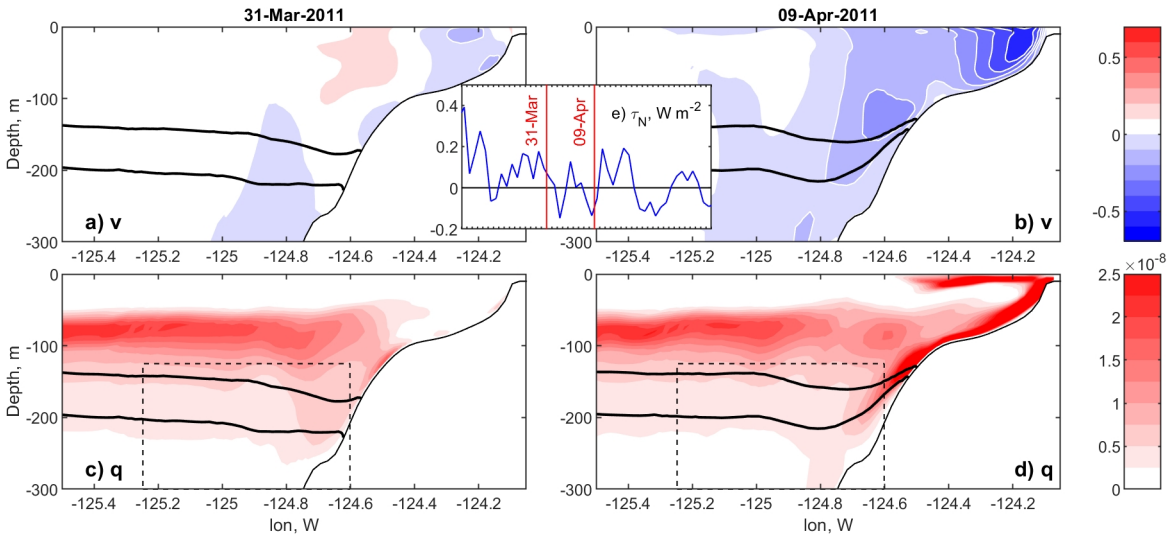

Figure 6. Cross-shore sections near the NH line of daily-averaged (TOP) meridional velocity component, m s^{-1}, (BOTTOM) potential vorticity q, s^{-3}; (LEFT) 31 March 2011, before the first upwelling event of the year, (RIGHT) 9 April 2011, following the peak of the upwelling event. Black contours are σ_θ = 26.25 and 26.5 kg m^{-3}. In (c)-(d), the dashed box is the slope area where v_s average is defined. (e) Daily-averaged meridional wind stress component (northward is positive) between 15 March - 1 May 2011, with red lines showing the dates selected for the cross-section plots.

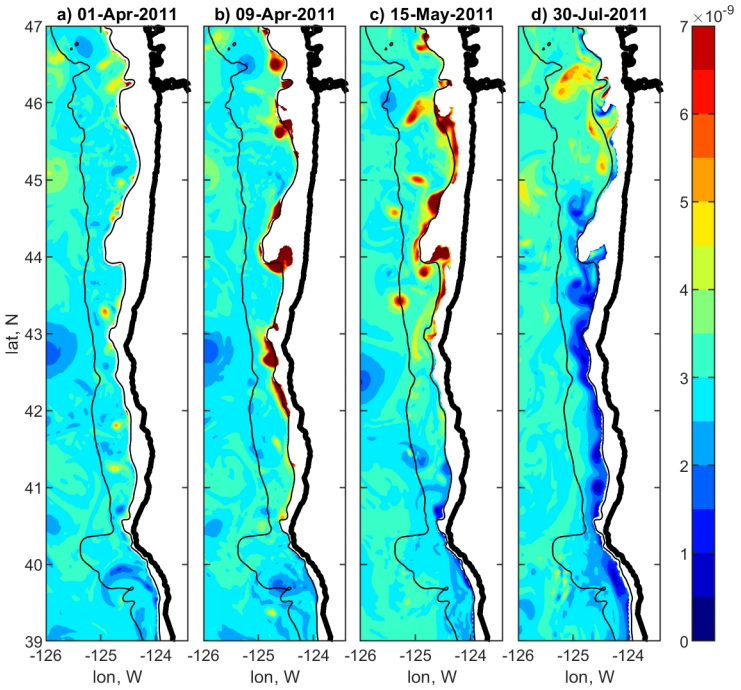

Figure 7. Maps of daily-averaged q (s^{-3}) on the isopycnal surface $\sigma_\theta = 26.5$ kg m^{-3} in the coastal area including Northern CA, all of Oregon and part of Washington State. Black contours are isobaths (200 and 2000 m).

year, the alongshelf current is low. At this time, q is relatively large in the interior at the depth of the winter pycnocline and is low over the shelf. With the onset of upwelling, as on Arpil 9, 2011 (Fig. 6b,d), q is large over the shelf. In this example, a tongue of high q is seen in the layer between the surfaces $\sigma_\theta = 26.25$ and 26.5 kg m^{-3} that will be transported later within that layer to the area over the slope. Maps of the daily-averaged q computed on $z_{26.5}$ (Figure 7) show relatively low q over the slope before the upwelling starts (Fig. 7a), followed by episodes of higher q transported with eddies from the shelf to the slope area following a series of upwelling events (b, c). The emerging undercurrent (c,d) is associated with the low q anomaly supported by the negative ω near the sloping bottom (Molemaker et al., 2015). Where the upwelling-related high and undercurrent-related low q meet, the largest $\partial q/\partial y$ is found. As the season progresses, the undercurrent "flushes" the slope waters in Oregon-Washington, pushing the high gradient area farther and farther north. Note that $\omega < -f$ is a condition for the onset of centrifugal instability (Haine & Marshall, 1998), such that $q > 0$ in Figure 7.

Pelland et al. (2013) studied coastal undercurrent eddies, or "cuddies" using glider hydrographic transects off the coast of Washington. They find that about one third of the cuddies detected in the ocean interior are anticyclonic and are associated with the patches of positive PV anomaly. Our model reproduces eddies similar to those anticyclonic cuddies (see Fig. 7). The relatively higher PV in these eddies is evidently of the shelf origin.

5 Term balance analysis for q_B

In this section it will be demonstrated that despite all the approximations that go into (4), it describes very well the seasonal evolution of the slope averaged q_B as well as the 2014 and 2015 summer anomalies. To summarize, the approximations include: (*i*) ω is neglected; (*ii*) q_B is the average PV in an area bounded by the two selected isopycnal surfaces and the horizontal extent of the slope band; (*iii*) v_s is used as the advective velocity, which is an average in a larger area that includes the selected isopycnal layer (see the dashed rectangle in Figure 6); (*iv*) the q flux from the shelf and the slope bottom and the offshore flux are ignored; (*v*) the alongshore filter is applied to both $v_s(y,t)$ and $q_B(y,t)$; (*vi*) daily-averaged values are utilized in the model that resolves the tides. In Figure 8, $TEND = \partial q_B/\partial t$ (half-tone) is compared to $ADV = -v_s \partial q_B/\partial y$ (red) at the NH latitude; the annual cycle in ADV (blue) is added for reference. $TEND$ is rather

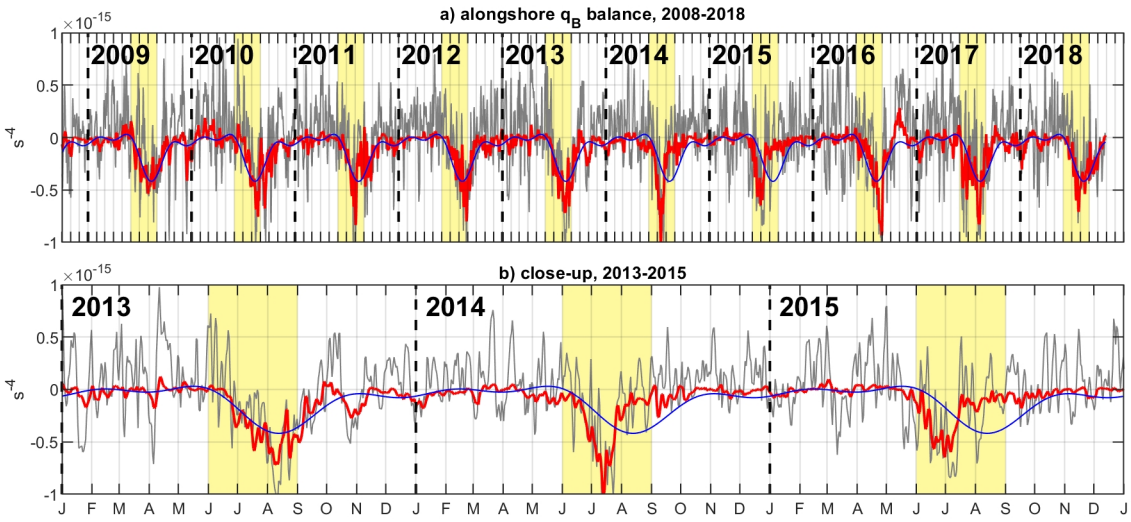

Figure 8. The PV term balance analysis over the slope at NH line: (gray) tendency $\partial q_B/\partial t$, (red) $ADV = -v_s \partial q_B/\partial y$, (blue) annual cycle in ADV (based on 2009-2013). (a) the entire 2008-2018 time period, (b) focus on 2013-2015. Vertical dashed lines: 1 January of each year. Yellow shades: summer months (JJA).

noisy as it is estimated from the daily values, but the drop to the strongly negative values is apparent every summer, associated with the passage of the high $\partial q_B/\partial y$ zone and the trail of the low q_B in the undercurrent. This pattern is followed very closely by ADV. In a close-up on 2013-2015 (Figure 8b), it is particularly clear that variability in 2013 is near average, which will be a staple of every year except 2014 and 2015. In those two years, ADV decreases and recovers about one or two months earlier than on average and $TEND$ follows the same pattern. It is not necessarily the stronger negative ADV but the earlier onset of the transition period that makes q_B anomalous in 2014 and 2015.

Next, each q_B and v_s can be written as a sum of the annual cycle and anomaly: $q_B = Q_B + q'_B$ and $v_s = V_s + v'_s$. At the NH location, it is confirmed that $\partial Q_B/\partial t$ closely follows $-V_s \partial Q_B/\partial y$ (not shown). Then,

$$\frac{\partial q'_B}{\partial t} \approx -V_s \frac{\partial q'_B}{\partial y} - v'_s \frac{\partial Q_B}{\partial y} - v'_s \frac{\partial q'_B}{\partial y}. \tag{5}$$

The narrative offered so far, that "the slope current anomaly carries the seasonal PV alongshore gradient" may suggest that the tendency on the lhs of (5) is mostly controlled by

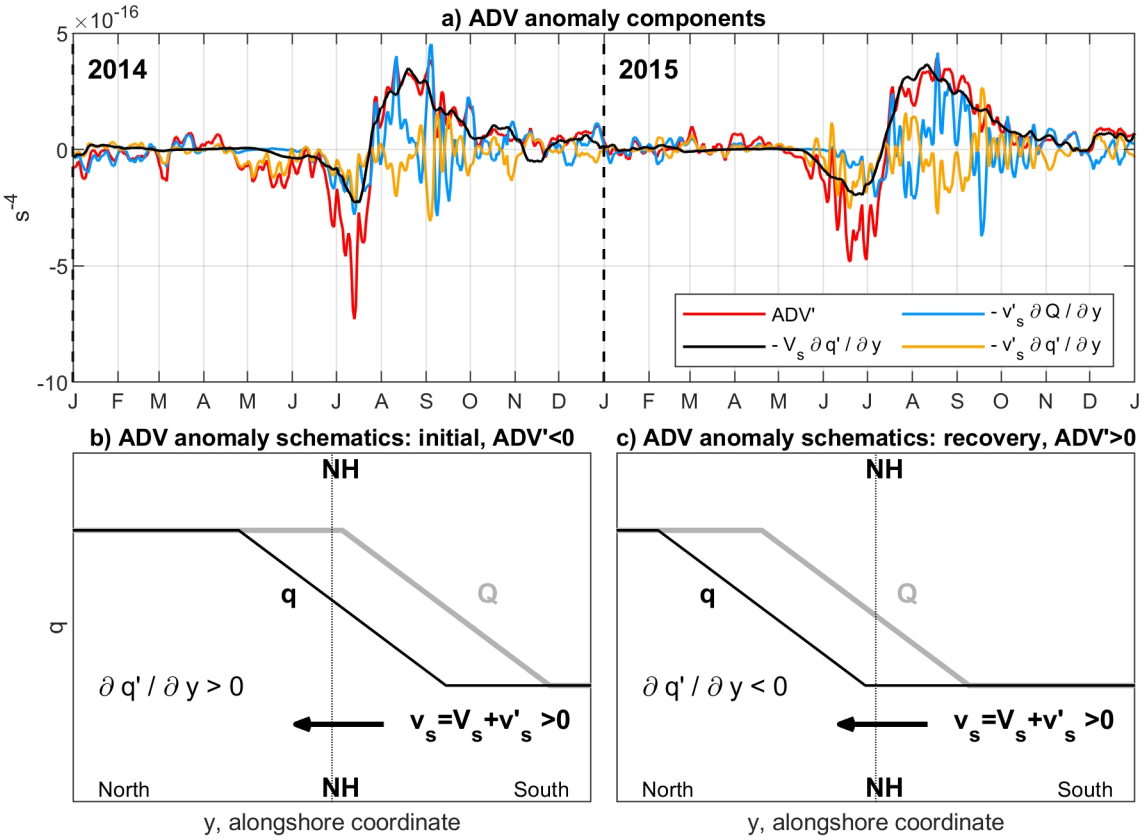

Figure 9. (a) Time series (2014-2015) of the (red) ADV anomaly and its contributing terms: (black) $-V_s\partial q'/\partial y$, (light blue) $-v_s'\partial Q/\partial y$, (orange) $-v_s'\partial q'/\partial y$, ; (b-c) schemes explaining the sign of each of the contributing terms to the ADV anomaly. At the initial phase, all the three contributing terms are negative. At the recovery phase, $\partial q/\partial y$ is small, thus $-v_s'\partial Q/\partial y$ and $-v_s'\partial q'/\partial y$ nearly balance each other.

the second term on the rhs. However, this is not the case (Figure 9a). In summer 2014 and 2015, the sum of the all the terms on the rhs of (5), ADV', goes first through the initial, negative phase followed by the positive recovery phase. At the initial phase all the three terms contribute equally to ADV'. At the recovery phase, term $-V_s\partial q'_B/\partial y$ follows closely ADV' and the other two terms on the rhs of (5) nearly balance each other. This behavior fully supports the assertion that the PV anomalies are caused by the earlier than usual advection of the strong PV front by the anomalously strong current. At the initial phase (Figure 9b), the zone of the strongest $\partial q/\partial y$ moves through section NH early, while $\partial Q/\partial y \approx 0$. Hence $\partial q'/\partial y > 0$ and the term $-v'_s\partial q'_B/\partial y$ initiates the negative anomaly in ADV'. The other two terms will eventually contribute, too, when V_s and $\partial Q/\partial y$ reach seasonal peaks. At the recovery phase, after the front has passed, $\partial q/\partial y = \partial Q/\partial y + \partial q'/\partial y \approx 0$ such that $-v'_s\partial Q_B/\partial y$ and $-v'_s\partial q'_B/\partial y$ nearly balance each other.

6 Concluding remarks

The regional ocean circulation model helps to discover and explain the events of anomalous stratification weakening in a layer over the slope off Oregon in July-August 2014 and 2015. The alongslope advection of the strong seasonal PV gradient earlier in the season than usual explains the PV tendency anomaly and hence the stratification anomaly. This anomaly is triggered by the anomalously strong (by as much as 0.1 m s^{-1}) and persistent alongslope current anomaly that arrives on the Oregon slope with the coastally trapped waves originating at the southern boundary and triggered by the El Niño oceanic mechanism.

As part of this study we also evaluated, but could not confirm, if the cross-shore PV flux anomalies also contribute to the stratification anomalies studied. The expectation was that the downwelling motion associated with the El Niño may provide an additional local source of negative PV anomaly over the slope. The downwelling is associated with the PV destruction over the slope (Bethuysen & Thomas, 2012) due to the geometric effect of the weakened stratification near the bottom. Enhanced mixing including convective instability (Moum et al., 2004) may also contribute to PV destruction during downwelling. There is also a possibility that the negative cross-shore velocity anomaly fluxes this PV deficit into the slope area. However, our analyses of the q flux across the 200-m isobath at the NH section (not shown) did not exhibit any strikingly anomalous behavior in the range of depths between $z_{26.5}$ and $z_{26.25}$ in summer 2014 or

2015. Two facts additionally point to the alongslope advection as the dominant mechanism explaning the stratification anomalies: (*i*) the q_B anomaly is found only where the seasonal $\partial Q/\partial y$ is large, and (*ii*) this anomaly, first appearing near Cape Mendocino in the Northern CA is displaced to the north with the speed characteristic of the poleward undercurrent.

While surface oceanic processes are well sampled by satellite sensors, subsurface flows remain undersampled. Availability of long-time continuous in-situ observational time series, similar to the CTD set used here, is very important for assessing dynamical processes on intraseasonal, seasonal, and interannual temporal scales. Accurate high-resolution models that show variability consistent with the sparse in-situ data remain important instruments to improve our understanding of subsurface flows, including in our case processes that define the shelf-interior ocean material and heat exchange.

Acknowledgments

We wish to thank Drs. K. Brink, P. MacCready, I. Rivin and J. Pringle for useful discussions. We are grateful to Jennifer Fisher for providing the CTD profile data. This research was partly supported by the NASA grant 80NSSC22K1003.

Data Availability Statement

CTD observations utilized in this study are available as described in (Risien et al., 2022). Model outputs and the entire model setup are freely available upon request to anybody interested in future analyses or developments.

References

Amaya, D. J., Bond, N. E., Miller, A. J., , & DeFlorio, M. J. (2016). The evolution and known atmospheric forcing mechanisms behind the 2013-2015 north pacific warm anomalies. *US Clivar Var.*, *14*, 1-6.

Austin, J. A., & Barth, J. A. (2002). Drifter behavior on the Oregon–Washington shelf during downwelling-favorable winds. *J. Phys. Oceanogr.*, *32*(11), 3132-3144.

Barth, J. A., Fram, J. P., Dever, E. P., Risien, C. M., Wingard, C. E., Collier, R. W., & Kearney, T. D. (2018). Warm blobs, low-oxygen events, and an eclipse: The Ocean Observatories Initiative endurance array captures them all.

Oceanography, *31*(1), 90-97. doi: 10.5670/oceanog.2018.114

Barth, J. A., & Smith, R. L. (1998). Separation of a coastal upwelling jet at cape blanco, oregon, usa. *S. Afr. J. Mar. Sci.*, *19*(1), 5-14. doi: 10.2989/025776198784126674

Bethuysen, J., & Thomas, L. N. (2012). Friction and diapycnal mixing at a slope: boundary control of potential vorticity. *J. Phys. Oce.*, *42*, 1509-1523. doi: 10.1175/JPO-D-11-0130.1

Bond, N. A., Cronin, M. F., Freeland, H., & Mantua, N. (2015). Causes and impacts of the 2014 warm anomaly in the ne pacific. *Geophys. Res. Lett.*, *42*, 3414–3420. doi: 10.1002/2015gl063306

Brink, K. H. (1991). Coastal-trapped waves and wind-driven currents over the continental shelf. *Ann. Rev. Fluid Mech.*, *23*, 389-412. doi: 10.1146/annurev.fl.23.010191.002133

Collins, C. A., Margolina, T., Rago, T. A., & Ivanov, L. (2013). Looping rafos floats in the california current system. *Deep Sea Res. Part II*, *85*, 42-61. doi: 10.1016/j.dsr2.2012.07.027

Connolly, T. P., Hickey, B. M., Shulman, I., & Thomson, R. E. (2014). Coastal trapped waves, alongshore pressure gradients, and the California undercurrent. *J. Phys. Oceanogr.*, *44*, 319-342. doi: 10.1175/JPO-D-13-095.1

Di Lorenzo, E., & Mantua, N. (2016). Multi-year persistence of the 2014/15 North Pacific marine heatwave. *Nature Clim. Change*, *6*, 1042-1048. doi: 10.1038/nclimate3082

Durski, S. M., & Allen, J. S. (2005). Finite-amplitude evolution of instabilities associated with the coastal upwelling front. *J. Phys. Oceanogr.*, *35*(9), 1606-1628. doi: 10.1175/JPO2762.1

Durski, S. M., Kurapov, A. L., Allen, J. S., Kosro, P. M., Egbert, G. D., Shearman, R. K., & Barth, J. A. (2015). Coastal ocean variability in the US Pacific Northwest region: seasonal patterns, winter circulation, and the influence of the 2009–2010 El Niño. *Oce Dyn*, *65*, 1643-1663. doi: 10.1007/s10236-015-0891-1

Egbert, G. D., & Erofeeva, S. Y. (2002). Efficient inverse modeling of barotropic ocean tides. *J. Atm. Oce. Tech.*, *19*(2), 183-204. doi: 10.1175/1520-0426(2002)019⟨0183:EIMOBO⟩2.0.CO;2

Fisher, J. L., Peterson, W. T., & Rykaczewski, R. R. (2015). The impact of El Niño events on the pelagic food chain in the northern California Current. *Global Change Biology*, *Global Change Biology*(21), 4401–4414. doi: 0.1111/gcb.13054

Garrett, C., MacCready, P., & Rhines, P. (1993). Boundary mixing and arrested Ekman layers: rotating stratified flow near a sloping boundary. *Ann. Rev. FLuid Mech.*, *25*, 291-323. doi: 10.1146/annurev.fl.25.010193.001451

Haine, T. W. N., & Marshall, J. (1998). Gravitational, symmetric, and baroclinic instability of the ocean mixed layer. *J. Phys. Oceanogr.*, *28*(634-658), 634-658. doi: 10.1175/1520-0485(1998)028⟨0634:GSABIO⟩2.0.CO;2

Hallberg, R., & Rhines, P. B. (2000). Boundary sources of potential vorticity in geophysical circulations. In R. M. Kerr & Y. Kimura (Eds.), *Developments in geophysical turbulence* (p. 51-65). Kluwer.

Haynes, P. H., & McIntyre, M. E. (1987). On the evolution of vorticity and potential vorticity in the presence of diabatic heating and frictional or other forces. *J. Atmos. Sci.*, *44*, 828-841.

Haynes, P. H., & McIntyre, M. E. (1990). On the conservation and impermeability theorems for potential vorticity. *J. Atmos. Sci.*, *47*, 2021-2031.

Hickey, B. M. (1998). Coastal oceanography of Western North America from the tip of Baja California to Vancouver Island. In K. H. Brink & A. R. Robinson (Eds.), *The Sea, Volume 11* (p. 345–393). Wiley and Sons, Inc., New York, NY.

Huyer, A. (1983). Coastal upwelling in the California current system. *Prog. Oceanogr.*, *12*(3), 259-284. doi: 10.1016/0079-6611(83)90010-1

Jacox, M. G., Desiree, T., Alexander, M. A., Hervieux, G., & Stock, C. A. (2019). Predicting the evolution of the 2014–2016 california current system marine heatwave from an ensemble of coupled global climate forecasts. *Front. Mar. Sci.*, *6*, 497. doi: 10.3389/fmars.2019.00497

Jacox, M. G., Hanzen, E. L., Zaba, K. D., Rudnick, D. L., Edwards, C. A., Moore, A. M., & Bograd, S. J. (2016). Impacts of the 2015–2016 el niño on the california current system: Early assessment and comparison to past events. *Geophys. Res. Lett.*, *43*, 7072-7080. doi: 10.1002/2016GL069716

Koch, A. O., Kurapov, A. L., & Allen, J. S. (2010). Near-surface dynamics of a

separated jet in the coastal tranzition zone off oregon. *J. Geophys. Res.*, *115*, C08020. doi: 10.1029/2009JC005704

Kosro, P. M., Huyer, A., Ramp, S. R., Smith, R. L., Chavez, F. P., Cowles, T. J., ... Small, L. F. (1991). The structure of the transition zone between coastal waters and the open ocean off northern California, winter and spring 1987. *J. Geophys. Res.*, *114*(C8), 14707– 14730. doi: 0.1029/91JC01210

Kurapov, A. L., Rudnick, D. L., Cervantes, B. T., & Risien, C. M. (2022). Slope and shelf flow anomalies off oregon influenced by the remote oceanic mechanism in 2014-16. *J. Geophys. Res.: Oceans*. doi: INPRESS

Kurapov, A. L., Rudnik, D. L., & Pelland, N. A. (2017b). Seasonal and interannual variability in along-slope oceanic properties off the US West Coast: Inferences from a high-resolution regional model. *J. Geophys. Res. Oceans,*, *122*, 5237–5259. doi: 10.1002/2017JC012721

MacCready, P., & Rhines, P. B. (1991). Buoyant inhibition of ekman transport on a slope and its effect on stratified spin-up. *J. Fluid Mech.*, *223*, 631–661. doi: 10.1017/S0022112091001581

MacCready, P., & Rhines, P. B. (1993). Slippery bottom boundary layers on a slope. *J. Phys. Oceanogr.*, *23*, 5-22. doi: 10.1175/1520-0485(1993)023⟨0005:SBBLOA⟩2.0.CO;2

Marshall, J. C., & Nurser, A. J. G. (1992). Fluid dynamics of oceanic thermohaline ventilation. *J. Phys. Oceanogr.*, *22*, 583-595.

McDowell, S., Rhines, P. B., & Keffer, T. (1982). North atlantic potential vorticity and its relation to the general circulation. *J. Phys. Oceanogr.*, *12*, 1417-1436.

McPhaden, M. J. (2015). Playing hide and seek with el niño. *Nature Clim Change*, *5*, 791-795. doi: https://doi.org/10.1038/nclimate2775

Molemaker, M. J., McWilliams, J. C., & Dewar, W. K. (2015). Submesoscale instability and generation of mesoscale anticyclones near a separation of the California undercurrent. *J. Phys. Oceanogr.*, *45*(3), 613-629. doi: 10.1175/JPO-D-13-0225.1

Moum, J. N., Perlin, A., Klymak, J. M., Levine, M. D., Boyd, T., & Kosro, P. M. (2004). Convectively driven mixing in the bottom boundary layer. *J. Phys. Oceanogr.*, *34*(10), 2189-2202. doi: 10.1175/1520-0485(2004)034⟨2189:CDMITB⟩2.0.CO;2

O'Dwyer, J., & Williams, R. G. (1997). The climatological distribution of potential vorticity over the abyssal ocean. *J. Phys. Oceanogr.*, *27*, 2488-2506.

Pedlosky, J. (1987). *Geophysical fluid dynamics*. Berlin: Springer. doi: 10.1007/978-1-4612-4650-3

Pelland, N. A., Eriksen, C. C., & Lee, C. M. (2013). Subthermocline eddies over the washington continental slope as observed by seagliders, 2003–09. *J. Phys. Oceanogr.*, *43*(10), 2025-2053. doi: 10.1175/JPO-D-12-086.1

Peterson, W. T., Fisher, J. L., Strub, P. T., Du, X., Risien, C., Peterson, J., & Shaw, C. T. (2017). The pelagic ecosystem in the northern california current off oregon during the 2014–2016 warm anomalies within the context of the past 20 years. *J. Geophys. Res. Oceans*, *122*, 7267–7290. doi: 10.1002/2017JC012952

Pierce, S. D., Smith, R. L., Kosro, P. M., Barth, J. A., & Wilson, C. D. (2000). Continuity of the poleward undercurrent along the eastern boundary of the mid-latitude north Pacific. *Deep-Sea Res. II*, *47*(5-6), 811-829. doi: 10.1016/S0967-0645(99)00128-9

Pringle, J. M. (2022). Instabilities in the bottom boundary layer reduce boundary layer arrest and stir boundary layer water into the stratified interior. *J. Geophys. Res.: Oceans*, *127*, e2021JC017253. doi: 10.1029/2021JC017253

Risien, C. M., Fewings, M. R., Fisher, J. L., Peterson, J. O., & Morgan, C. A. (2022). Spatially gridded cross-shelf hydrographic sections and monthly climatologies from shipboard survey data collected along the Newport Hydrographic Line, 1997–2021. *Data in Brief*, *41*, 107922. doi: 10.1016/j.dib.2022.107922

Rudnick, D. L., Owens, W. B., Johnston, T. M. S., Karnauskas, K. B., Jakoboski, J., & Todd, R. E. (2021). The equatorial current system west of the Galápagos Islands during the 2014–16 El Niño as observed by underwater gliders. *J. Phys. Oceanogr.*, *51*, 3-17. doi: 10.1175/JPO-D-20-0064.1

Samelson, R. M. (2017). Time-dependent linear theory for the generation of poleward undercurrents on eastern boundaries. *J. Physic. Oceanogr.*, *47*(12), 3037–3059. doi: 10.1175/JPO-D-17-0077.1

Thomas, L. N. (2005). Destruction of potential vorticity by winds. *J. Phys. Oceanogr.*, *35*, 2457-2466. doi: 10.1175/JPO2830.1

Williams, R. G., & Roussenov, V. (2003). The role of sloping sidewalls in forming

potential vorticity contrasts in the ocean interior. *J. Phys. Oceanogr.*, *33*, 633-648.

Zaba, K. D., & Rudnick, D. L. (2016). The 2014–2015 warming anomaly in the southern california current system observed by underwater gliders. *Geophys. Res. Lett.*, *43*, 1241-1248. doi: 10.1002/2015GL067550

Zaba, K. D., Rudnick, D. L., Cornuelle, B. D., Gopalakrishnan, G., & Mazloff, M. R. (2020). Volume and heat budgets in the coastal California Current system: means, annual cycles, and interannual anomalies of 2014–16. *J. Phys. Oceanogr.*, *50*, 1435-1436. doi: 10.1175/JPO-D-19-0271.1